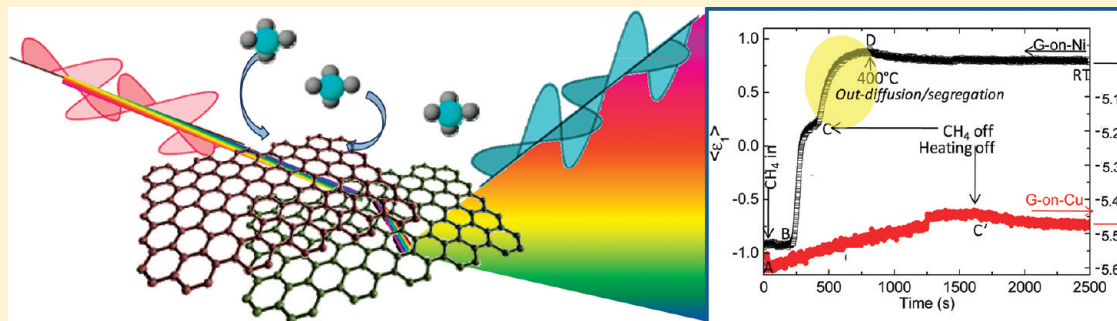


# Ellipsometry as a Real-Time Optical Tool for Monitoring and Understanding Graphene Growth on Metals

Maria Losurdo,\* Maria M Giangregorio, Pio Capezzuto, and Giovanni Bruno

Institute of Inorganic Methodologies and of Plasmas, National Council of Research, IMIP-CNR, via Orabona 4, 70126 Bari, Italy

Supporting Information

**ABSTRACT:**

Despite the recent advances in the chemical vapor deposition (CVD) of graphene, it is still a great challenge to control the thickness of graphene especially in real-time during the growth. So far, there are no reports on the real-time monitoring of graphene growth. Here, we show for the first time real-time in situ kinetic monitoring of graphene deposition by CVD on nickel. We demonstrate an optical nondestructive method of dynamic spectroscopic ellipsometry for controlling and optimizing the catalyst cleaning and annealing and, consequently, the graphene deposition and properties. The kinetic ellipsometry monitoring also highlights the mechanism of graphene formation. Discussion shows the applicability and industrial scalability of this ellipsometric method to the control of large-area graphene formation on any substrate. This approach opens a way to in-line real-time graphene metrology and is helpful in guiding the graphene growth process as we try to achieve reproducible and controllable research as well as industry processes for quality graphene formation.

**INTRODUCTION**

Graphene is the subject of intense research activity aimed at exploiting its unique properties to establish a technological platform for applications in electronics<sup>1–3</sup> and sensing.<sup>4</sup> The exfoliation of graphite<sup>5</sup> provided a reference quality material for graphene properties and is still the method for producing free-standing graphene as an ideal two-dimensional material and allowing its properties to be investigated. With the aim of achieving large-area growth of high-quality graphene, advancements are being made at a rapid pace in various synthesis approaches, including epitaxy on SiC,<sup>6</sup> chemical reduction of graphite oxide,<sup>7</sup> and chemical vapor deposition (CVD) on transition metals like copper (Cu) and nickel (Ni).<sup>8–12</sup>

Indeed, as engineering applications of graphene layers attract increasing interest, we need to develop some form of in situ control of graphene deposition in order to improve graphene properties. One way of modifying the electrical and optical properties is to change the number of graphene layers. Therefore, a mandatory step toward achieving control and repeatability of graphene growth is certainly opening the way to monitoring the thickness of graphene, especially in real-time during the growth. So far, for all the above-mentioned synthetic routes to graphene,

there are no reports on approaches to real-time controlled growth, which represents an essential prerequisite for the fabrication of integrated device architectures. Controlling or at least inferring the thickness of graphene in real-time during its formation is quite challenging, especially when graphene is deposited on polycrystalline metal catalysts via segregation/precipitation, which is an extremely complex process to understand and control also because of the interface heterogeneity and grain boundaries characterizing the substrate.

Here we demonstrate for the first time a nondestructive real-time spectroscopic ellipsometry (SE)<sup>13</sup> optical metrology technique to monitor graphene growth in-line, correlating process kinetics with its thickness and properties. The advantage of this nondestructive and nonintrusive optical characterization is that it can be applied to detect a few monolayers of graphene on any substrate, transparent (like SiC) as well as opaque (like metals), and therefore it is fully extendable and well suited to monitor in real-time graphene formation either during epitaxy on SiC or on

Received: July 19, 2011

Revised: September 1, 2011

Published: September 30, 2011

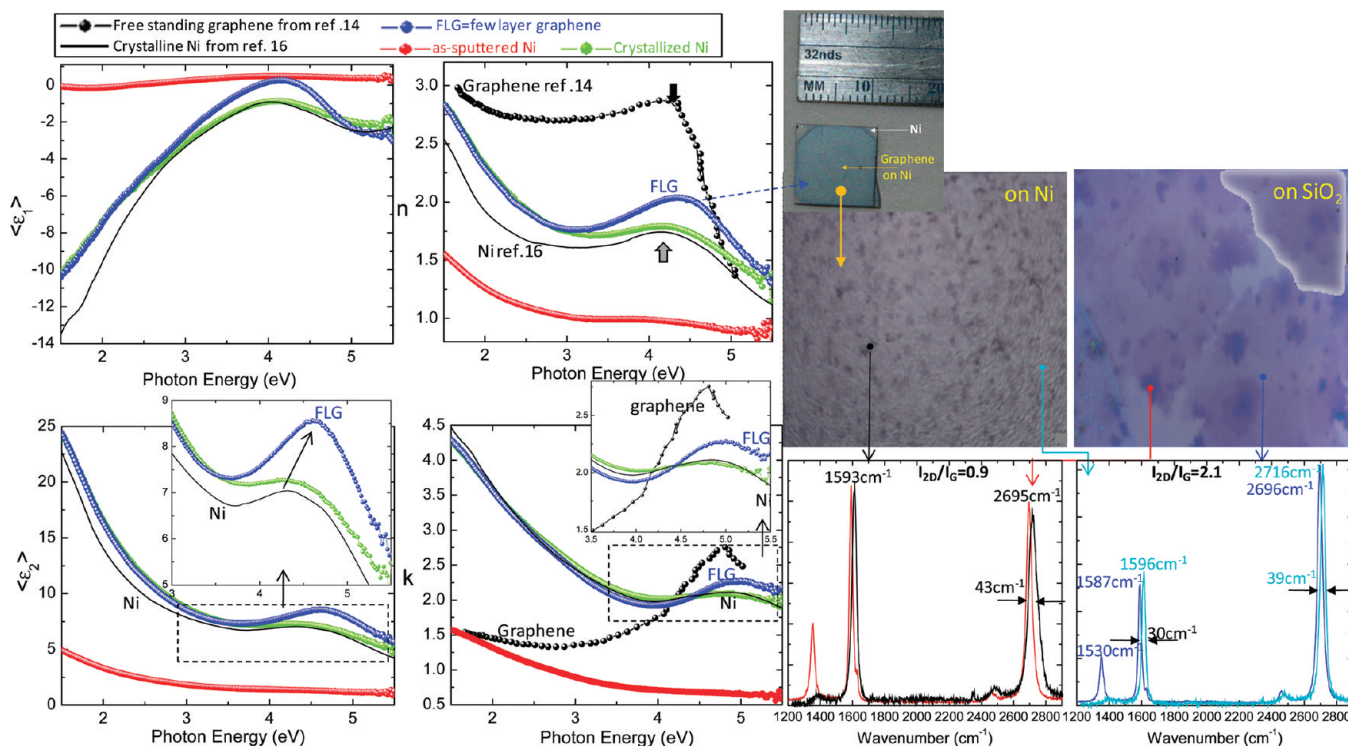


**Figure 1.** (a) Spectra of the real,  $\langle \epsilon_1 \rangle$ , and imaginary,  $\langle \epsilon_2 \rangle$ , parts of the pseudodielectric function and of the refractive index,  $n$ , and extinction coefficient,  $k$ , of the as-sputtered 300 nm Ni/300 nm SiO<sub>2</sub>/Si substrate (red curve) of the annealed Ni substrate (green curve) and of a typical few-layers graphene (FLG) on Ni (blue curve) compared to that of exfoliated graphene from ref 14 (black dots) and of reference Ni from ref 16 (black line). The insets are a magnification of the spectral region above 3 eV. (b) Photograph of a FLG on Ni sample. (c) Optical microscopy images of as-grown FLG on Ni (600  $\mu\text{m} \times 600 \mu\text{m}$ ) and after transferring to 300 nm SiO<sub>2</sub>/Si (300  $\mu\text{m} \times 300 \mu\text{m}$ ). (d) Raman spectra acquired in light (cyano) and dark (black) regions of the FLG on Ni and after transferring to SiO<sub>2</sub> (blue spectrum in light region and red spectrum in darker regions).

a metal catalyst. In this paper, we show mainly the case of CVD of graphene on Ni to provide guidelines for its application.

Recently Kravets et al.<sup>14</sup> have reported the optical constant of a monolayer of exfoliated graphene supported on a SiO<sub>2</sub>/Si wafer, assuming a thickness of 3.35 Å in the analysis. Nelson et al.<sup>15</sup> also reported the optical properties for CVD graphene after transferring it to a glass substrate; a thickness of 3.35 Å was also assumed in fitting SE data to extract the isotropic optical constant of monolayer graphene. These previous studies have set reference optical properties for transferred graphene monolayers, which are exploited in the present study to monitor, for the first time, the graphene growth process, discuss and determine the effect of the interaction with the substrate on the optical response of CVD graphene, and infer information about the kinetics and mechanism of graphene CVD deposition. Therefore, our approach provides a practical and exploitable way for advancing the “blind” growth of graphene.

## EXPERIMENTAL SECTION

**Sample Preparation and Experimental Setup.** Graphene was grown by chemical vapor deposition (CVD) from a mixture of CH<sub>4</sub>:H<sub>2</sub> = 100:50 sccm gases at a temperature of 900 °C and at a total pressure of 4 torr in a stainless-steel CVD reactor. Growth times between 2 and 15 min were used to vary the thickness of the few-layer graphene (FLG) between approximately 3 and 25 Å (this is an optical equivalent thickness, corresponding to Raman analysis showing between 1 and 8 layers). The sample is then cooled at a rate of  $\sim 2$  °C/min in 1 torr of H<sub>2</sub>.

The substrate used was 300 nm Ni/300 nm SiO<sub>2</sub>/Si obtained by Ni sputtering. It was preannealed at 400 °C in UHV for nickel oxide desorption for a time of 5–15 min and then heated to 900 °C in 1 torr of H<sub>2</sub> over a period of  $\sim 40$ –60 before addition of methane. (See Figure S1 in the Supporting Information for a picture of the experimental setup.)

**Spectroscopic Ellipsometry.** Spectroscopic ellipsometry<sup>13</sup> monitored in real-time the growth by directly recording the pseudodielectric function  $\langle \epsilon \rangle = \langle \epsilon_1 \rangle + i\langle \epsilon_2 \rangle$  of the metal catalyst as well as of graphene layers, which is related to the extinction coefficient  $\langle k \rangle$  and refractive index  $\langle n \rangle$  of materials by the following equation

$$\langle \epsilon \rangle = \langle \epsilon_1 \rangle + i\langle \epsilon_2 \rangle = \sin^2 \phi \left[ 1 + \tan^2 \phi \frac{(1 - \rho)^2}{(1 + \rho)^2} \right] = \langle (n + ik)^2 \rangle$$

where  $\phi$  is the angle of incidence fixed at 70° and  $\rho$  is the complex reflection coefficient for the parallel,  $p$ , and perpendicular,  $s$ , polarizations, defined as

$$\rho = \frac{r_p}{r_s} = \tan \Psi \cdot e^{i\Delta}$$

where  $\tan \Psi$  represents the change of amplitude of the reflected polarized light beam with respect to the linearly polarized incident beam, while the phase change between the two polarizations is related to  $\cos \Delta$ . Details are better described in the Supporting Information. Ellipsometric spectra were acquired every 1 s using a phase-modulated spectroscopic ellipsometer (UVISSEL, Horiba Jobin Yvon) in the 0.75–6.5 eV spectral range

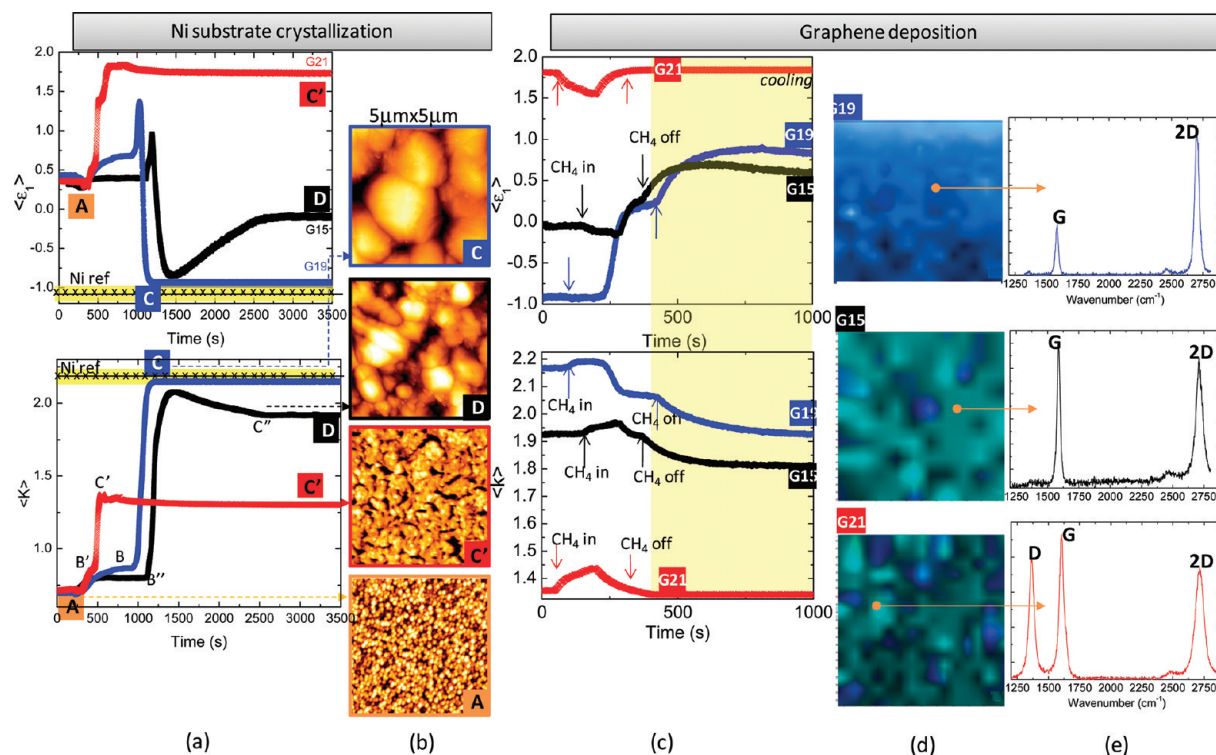


**Figure 2.** (a) Real-time evolution of  $\langle \epsilon_1 \rangle$  and  $\langle k \rangle$  monitored at the photon energy of 4.2 eV during annealing of the 300 nm Ni/300 nm  $\text{SiO}_2/\text{Si}$  substrate in  $\text{H}_2$ . (b) Corresponding  $5 \mu\text{m} \times 5 \mu\text{m}$  AFM topography images recorded for the three Ni substrates annealed at different temperature. (c) Real-time  $\langle \epsilon_1 \rangle$  and  $\langle k \rangle$  evolution monitored at the photon energy of 4.2 eV during graphene growth on the three characteristics Ni substrates; the time when  $\text{CH}_4$  is flowed and stopped are also indicated; the yellow region indicates cooling down of the sample from 900 °C to room temperature in  $\text{H}_2$ . (d) Raman  $100 \mu\text{m} \times 100 \mu\text{m}$  maps of the  $I_{2D}/I_G$  intensity ratio for FLG samples corresponding to the various kinetics and (e) Raman spectra acquired in characteristic points indicated by the yellow dot. Blue region corresponds to monolayer graphene; green region to 2–3 layers graphene, and light green to >3 layers graphene.

with a 0.01 eV resolution. Analysis of the ellipsometric spectra to extract the optical constant of the graphene layers requires the application of an appropriate optical model to fit experimental data. The model used consisted of a one-layer model (substrate/graphene/air). Fit variables in this model are the thickness and the parametrization for the optical constant of graphene.

(For completeness, more details on ellipsometric analysis can be found in the Supporting Information.)

**Raman Spectroscopy.** Raman spectroscopy has shown to be a powerful tool to assess thickness and quality of graphene layers. Raman spectra were then collected using a LabRAM HR Horiba-Jobyn Yvon spectrometer with 532 nm excitation under ambient conditions at low laser power (<1 mW) to avoid laser-induced damage using a Horiba Jobin-Yvon LabRAM HR spectrometer. Raman mapping with a  $1 \mu\text{m}$  resolution was also run.

**Atomic Force Microscopy.** AFM was performed in the intermittent-contact mode (IC-AFM) using an AutoProbe CP Thermomicroscope. A high aspect ratio probe super-sharp tip with a radius of curvature of 2 nm (ESP Series Probes-VEECO) was used.

## RESULTS AND DISCUSSION

Few-layer graphene (FLG) was grown by low-pressure CVD (LPCVD) at a temperature of approximately 900 °C using  $\text{CH}_4/\text{H}_2$  mixtures on a polycrystalline nickel (Ni) catalyst. The growth was preceded by annealing at 900 °C in  $\text{H}_2$  of the Ni substrate to facilitate development of crystallized Ni as a template for

graphene growth, as described in detail in the methods section and in the Supporting Information. For comparison, samples were also grown on polycrystalline copper (Cu) under the same experimental conditions. All steps of the graphene growth were monitored in real-time by spectroscopic ellipsometry, directly recording the pseudodielectric function  $\langle \epsilon \rangle = \langle \epsilon_1 \rangle + i\langle \epsilon_2 \rangle$ , which is related to the pseudoextinction coefficient  $\langle k \rangle$  and refractive index  $\langle n \rangle$  of the growing graphene. (See methods section and Supporting Information for details on methodology.)

Figure 1 summarizes the spectra of the main optical properties, i.e., the real,  $\langle \epsilon_1 \rangle$ , and imaginary,  $\langle \epsilon_2 \rangle$ , parts of the pseudodielectric function, the refractive index,  $n$ , and extinction coefficient,  $k$ , of the initial as-sputtered Ni substrate, of the annealed Ni substrate, and of a typical few-layer graphene (FLG) sample grown on Ni. For comparison, the refractive index and extinction coefficient of free-standing graphene<sup>14</sup> obtained by exfoliation are also shown.

In order to assess the quality of the graphene samples on which this study is demonstrated, a typical photograph as well as an optical microscope image and Raman spectra measured in different regions of the of the graphene, directly on Ni and after transferring to a 300 nm  $\text{SiO}_2/\text{Si}$  substrate, are also shown. The lightest gray regions show a full width at half-maximum (fwhm) ( $39 \text{ cm}^{-1}$ ) and a single symmetric Lorentzian line shape profile peaked at  $2716 \text{ cm}^{-1}$  (on Ni) and at  $2696 \text{ cm}^{-1}$  (on  $\text{SiO}_2$ ) of the 2D band, with a 2D-to-G intensity ratio  $I_{2D}/I_G \sim 2.1$  corresponding to a monolayer or bilayer graphene, covering up to 80% over  $22\,500 \mu\text{m}^2$ . Dark gray regions are few-layer (L) graphene

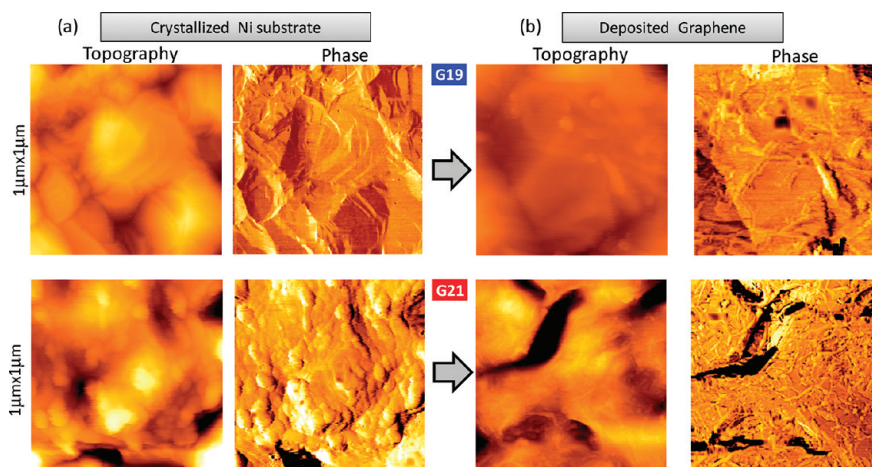


**Figure 3.** AFM topography ( $1 \mu\text{m} \times 1 \mu\text{m}$ ) and phase images for the (a) crystallized Ni substrate and (b) corresponding graphene layers deposited on top for the samples G19 and G21 of Figure 2.

with  $L > 3$  as indicated by the Raman spectrum showing a  $I_{2D}/I_G \sim 0.9$  and a 2D fwhm of  $43 \text{ cm}^{-1}$ . The D peak at  $1530 \text{ cm}^{-1}$  associated to defects is absent for the as-grown graphene on Ni, while it appears after transferring to  $\text{SiO}_2$ .

This overall comparison of spectra allows identification of the spectral region sensitive to the graphene formation, which is the region above 4 eV, where graphene shows an absorption peak at 4.6 eV due to a van Hove singularity in the graphene density of states<sup>14,15</sup> (indicated by the black arrow in Figure 1). For comparison, literature values of dielectric constants of a clean and crystalline nickel<sup>16</sup> at room temperature are also given in Figure 1. Furthermore, the dielectric function/complex refractive index of the polycrystalline Ni described in this paper is very similar to that observed for thinner Ni films in a previous experimental work.<sup>18</sup> The nickel also shows a main peak near 4.6 eV due to transitions from the lowest d-band to a free-electron-like band along all the three directions  $\Lambda$ ,  $\Delta$ , and  $\Sigma$  in the Brillouin zone<sup>17</sup> (also indicated by the gray arrow in Figure 1), while the Drude free-electron absorption of Ni predominates in the spectral region below 3 eV. The vicinity of the two main inter-band optical transitions of graphene and Ni renders measuring graphene on Ni challenging; nevertheless, the data reported in the inset of Figure 1a, indicating that the energy and amplitude of the graphene transition also depend on the number of graphene layers, show that there is enough sensitivity to monitor graphene formation also on Ni.

Figure 1 shows that the larger refractive index and absorption of graphene above 4 eV provide sensitivity to graphene formation. Therefore, this plot gives evidence and a guideline that even a green-blue laser single-wavelength ellipsometry system is suitable for industry to control in real-time graphene growth.

Furthermore, the different optical properties for the “as-sputtered” Ni substrate, which is amorphous, of the polycrystalline Ni, and of the graphene provide sufficient sensitivity to monitor all the steps involved in the graphene growth process, starting from the Ni catalyst cleaning—annealing—crystallization process. Specifically, Figure 2 summarizes the impact of the Ni cleaning/crystallization dynamics on the growth and properties of graphene. Here, the effect of the temperature during the Ni annealing kinetics in  $\text{H}_2$  for three initially identical Ni substrates monitored at the photon energy of 4.2 eV (close to the van Hove singularity point of Ni and graphene) is mainly described.

Knowing that we are starting from an amorphous Ni layer, the objective is to set a Ni processing able to yield a crystallized substrate, whose dielectric function matches that of a reference crystalline Ni sample. With reference to data in Figure 1, this implies that the optical guideline to monitor and optimize the cleaning/crystallization is setting processing conditions leading to Ni the reference values of  $\epsilon_1 = -1.02$  and  $k = 2.1$  at the probing photon energy. Specifically, in Figure 2, sample G21 was annealed directly at  $900 \text{ }^\circ\text{C}$  sample, while G19 was kept for 15 min at  $400 \text{ }^\circ\text{C}$  in  $\text{H}_2$  (A–B), before increasing the temperature to  $900 \text{ }^\circ\text{C}$  (B–C), and sample G15 was annealed at  $300 \text{ }^\circ\text{C}$  also for 15 min (A–B’’) before annealing at  $900 \text{ }^\circ\text{C}$  (however, also a longer time of 30 min was checked to be sure that we were anyway analyzing temperature-induced saturation phenomena). In all cases, for a reliable comparison, the total annealing time was 1 h. The black crossed lines (labeled as Ni-ref) indicate the optical guideline value that should be reached for crystallized cleaned Ni surfaces. The full range spectra are shown in the Supporting Information (Figure S3) in comparison also with a reference crystalline Ni surface spectrum, confirming that the G19 Ni surface is the closest to that of a cleaned and crystallized Ni, therefore supporting the statement that the higher the  $\langle k \rangle$  value and the lower the  $\langle \epsilon_1 \rangle$  value, the better the Ni substrate.

The Ni reference values are reached for sample G19, indicating that a preliminary step of slow annealing at  $400 \text{ }^\circ\text{C}$  promotes a better Ni crystallization. The unexpected very low value of  $\langle k \rangle$  and high value of  $\langle \epsilon_1 \rangle$  for sample G21 (which was quickly ramped up to  $900 \text{ }^\circ\text{C}$ , skipping the intermediate 10 min annealing at  $400 \text{ }^\circ\text{C}$ ) indicates that a high-temperature annealing, even for a long time, is not a sufficient condition to obtain a Ni surface suitable for graphene deposition. Indeed, another factor to be considered is the removal of native oxide from the Ni catalyst before the crystallization process, according to the following process:



Interestingly,  $300\text{--}400 \text{ }^\circ\text{C}$  has been reported to be the reduction temperature of NiO.<sup>19,20</sup> The high-magnification phase AFM images for samples G19 and G21, reported in Figure 3, indicate that sample G21 is formed by agglomerates of smaller grains that have not completely fused despite the prolonged  $900 \text{ }^\circ\text{C}$

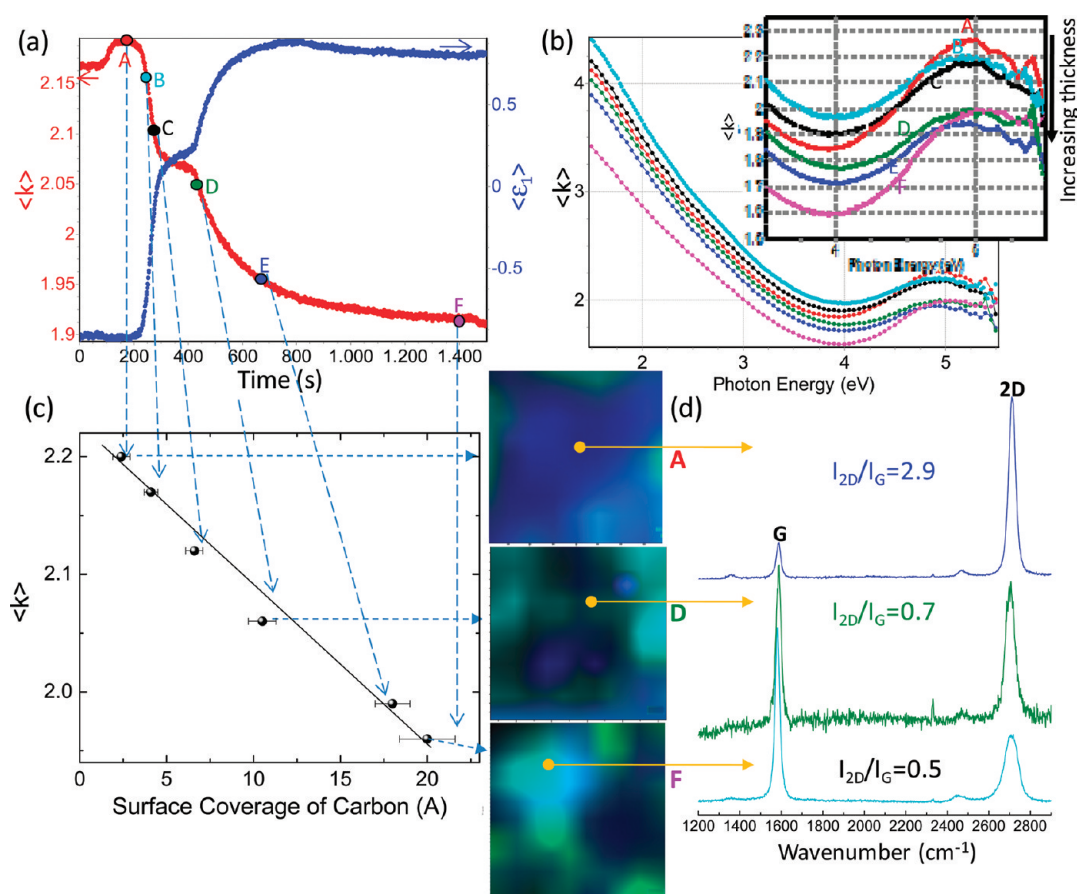


**Figure 4.** (a) Real-time kinetic profiles of  $\langle k \rangle$  and  $\langle \epsilon_1 \rangle$  recorded at the photon energy of 4.2 eV during graphene growth. (b)  $\langle k \rangle$  spectra recorded at some representative points and fit to extract the equivalent surface carbon optical thickness. (c) Correlation between the  $\langle k \rangle$  value and the surface coverage of carbon in equivalent optical thickness to be used for the real-time control of FLG. (d) Raman maps ( $10 \mu\text{m} \times 10 \mu\text{m}$ ) of the  $I_{2D}/I_G$  intensity ratio with some representative Raman spectra at the indicated points, indicating the correlation between the in-line  $\langle k \rangle$  value and ex situ Raman spectra.

annealing. Conversely, a longer preannealing time at 400 °C (sample G19) allows these formed Ni clusters to grow two-dimensionally across the surface until they overlap. It is also noted that many of the large particles were very angular in form and showed internal structure which appeared to be twin planes. X-ray diffraction data showed that the larger islands are now also faceted parallel to the [100] and [010] directions, consistently with data in ref 21. Thus, the preannealing at 400 °C favors desorption of the nickel oxide, leading to the formation of flat faceted micrometer-size grains with a lower root-mean-square roughness. On the other hand, the incomplete removal of the nickel oxide, when the preannealing is run rapidly, inhibits grain coalescence. This is consistent with fundamental studies of the hydrogen reduction of NiO, which is characterized by an induction period and time dependence, which are functions of the temperature;<sup>22</sup> i.e., the lower the temperature, the longer the induction time for NiO reduction. Koga and Harrison<sup>23</sup> represented the reduction process of NiO in hydrogen as the generation of nickel atoms on the outer surface of NiO grains. Following this metallic Ni nucleation, Ni clusters grow two-dimensionally across the surface until they overlap; the metallic Ni promotes rapid dissociation of hydrogen that diffuses into the grains allowing further reduction of the residual NiO.

Therefore, shorter preannealing times cause an intermediate stage of reduction of NiO and discrete grainy islands (assembly

of Ni grains), originating from the sintering of partially reduced Ni forming on still nonreduced NiO nanoparticles. This incomplete reduction of NiO affects the subsequent graphene growth kinetics and quality, as will be shown below.

Furthermore, a long annealing time in  $\text{H}_2$  is thought to result in larger grains and less grain boundaries. However, it should be considered that when evaporated nickel films are annealed for a long time in molecular hydrogen, hydrogen dissolves in nickel forming an anisotropic  $\alpha$  solid nickel-hydride solution.<sup>24</sup> The real-time kinetic trace in Figure 2 for sample G15 shows that after a critical time, once the  $\langle \epsilon_1 \rangle$  minimum and  $\langle k \rangle$  maximum are reached (point C' in Figure 2), the trend reverses and a decrease of  $\langle k \rangle$  and increase of  $\langle \epsilon_1 \rangle$  are observed (C'–D), which indicates a deviation from a metallic-Ni behavior, corresponding to a significant Ni-hydride phase. After the transformation of the nickel film into its hydride phase, the Ni catalytic activity of  $\text{CH}_4$  decomposition and dehydrogenation decreases considerably,<sup>25</sup> affecting in an uncontrolled way carbon solubility and graphene formation. Therefore, it is important to detect the Ni optimal crystallization point, avoiding large Ni-hydride formation.

Thus, we have shown the importance of the real-time optical detection of the Ni cleaning and crystallization end point (point C in Figure 2), which allows the avoidance of incomplete NiO reduction and large Ni-hydride phase formation. Also, these data show the high sensitivity of  $\langle \epsilon_1 \rangle$  and  $\langle k \rangle$  in monitoring the quality

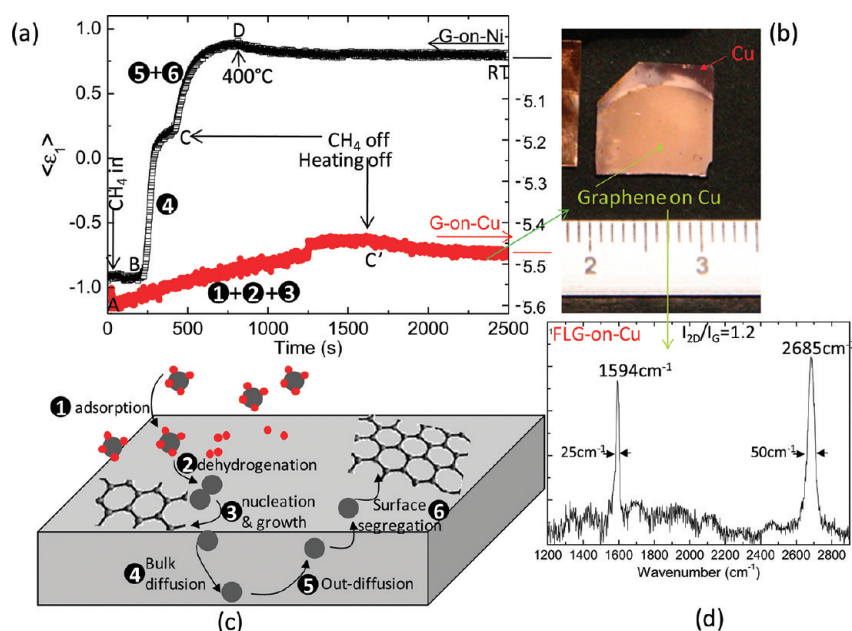


**Figure 5.** (a) Real-time kinetic profiles of the real part,  $\langle \epsilon_1 \rangle$ , of the pseudodielectric function recorded at the photon energy of 4.2 eV during graphene growth on polycrystalline 300 nm Ni/300 nm SiO<sub>2</sub>/Si (black curve) and on polycrystalline 300 nm Cu/300 nm SiO<sub>2</sub>/Si (red curve); at A-point CH<sub>4</sub> is injected into reactor, at C-point CH<sub>4</sub> is stopped and sample cooled down, at D-point temperature reached 400 °C, and the final point is at room temperature (RT). (b) Photograph of the FLG grown on copper. (c) Sketch of graphene formation by both direct chemisorptions/deposition and precipitation/segregation. (d) Typical Raman spectrum of FLG on copper.

of the Ni surface and its suitability to the subsequent graphene deposition. In fact, a direct correlation exists between the Ni catalyst characteristics and the graphene deposition kinetics and quality, as shown in the right panel of Figure 2.

Specifically, those three characteristic substrates were exposed to CH<sub>4</sub>–H<sub>2</sub> under the same experimental conditions for the graphene growth, and the corresponding real-time kinetic traces during graphene formation are shown. Different kinetics are observed depending on the status of the Ni catalyst, which result in a different final quality/thickness of the graphene layers as indicated by the Raman spectra and of the  $I_{2D}/I_G$  intensity ratio maps reported in the same Figure 2.

Scanning the 1 cm<sup>2</sup> samples with Raman spectroscopy, we always detect the 2D peak, indicating continuity of the film over the whole area. To further evaluate the impact of growth process on the thickness distribution of graphene, we run Raman mapping over a 100 μm<sup>2</sup> area. The variation of color contrast indicates that the film is not uniform in thickness and consists of different mixtures of single- and few-layer regions with a lateral size in the range of 50–100 μm. The distribution of these monolayer or few-layers graphene domains is related to the Ni catalyst surface quality. Indeed, this correlation and final graphene quality can be inferred in real-time by the optical real-time spectra.

Specifically, it can be inferred that very low  $\langle k \rangle$  spectra for the Ni substrate lead to nonhomogeneous thickness and defected graphene, while  $\langle k \rangle$  spectra coincident with the Ni reference lead to the possibility of controlling the thickness of graphene at mono- and bilayer level.

It is worth noticing that when the real-time optical graphene growth kinetics is G19-like, the Raman spectra for the graphene on Ni show only the G band at  $\sim 1596$  cm<sup>-1</sup> and the 2D band at  $\sim 2716$  cm<sup>-1</sup> with a peak intensity ratio  $I_{2D}/I_G \sim 3$  and a fwhm of the 2D peak ranging from 39 cm<sup>-1</sup> (dark blue) to 42 cm<sup>-1</sup>

(light blue region), indicating the absence of defects in the as-grown monolayer graphene, when optimized Ni processing is run. The blue shift of the G and 2D bands for graphene grown on Ni compared to exfoliated graphene can be understood by the strain effect caused by the interaction between the Ni substrate and graphene, consistently with values reported by other CVD growths on Ni.<sup>26</sup>

Comparison of Raman color maps in relation to the optical monitoring of both Ni processing and subsequent graphene growth reveal that larger nonuniformity, larger 2D peak widths and smaller  $I_{2D}/I_G$  ratios are observed for very low optical quality of the Ni catalyst. The D band, indicative of defects, is observed only when the Ni catalyst is not well cleaned and/or crystallized (associated to G21-like kinetics), as also supported by the higher number of wrinkles and ripples in the AFM of Figure 3.

Therefore, the real-time ellipsometry kinetics provide an effective way to control and infer the substrate and graphene quality.

The issue relating to the real-time control of the FLG graphene thickness, through the control of the carbon coverage, is shown in Figure 4. Here, the graphene growth kinetics during exposure of the optimal crystallized Ni surface to CH<sub>4</sub>–H<sub>2</sub> is shown together with corresponding ellipsometric spectra for several fluxing times (indicated by the colored dots on the kinetic profile). The fit analysis yields the coverage of the surface by carbon in equivalent thickness (we prefer to use this term instead of thickness of graphene, since samples on the large area of the spot of the ellipsometer, 6 × 4 mm<sup>2</sup>, have nonhomogeneous regions with different numbers of graphene layers). It can be seen that the higher the  $\langle k \rangle$  value, the lower the coverage of carbon and the larger the regions of the monolayer graphene; the number of layers increases with the carbon coverage as cross-corroborated by the Raman analysis and maps, also shown in Figure 4. Specifically, a correlation between the  $\langle k \rangle$  value and the carbon

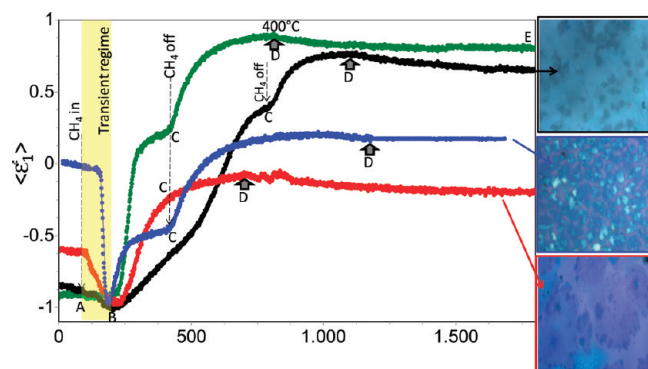


**Figure 6.** Real-time kinetics for graphene growth on Ni substrates preannealed at 400 °C for different times in the range 5–20 min (blue curve, 5 min; red curve, 10 min; green curve, 15 min; black curve, 20 min). At the A-point CH<sub>4</sub> is introduced into the reactor; at the C-point CH<sub>4</sub> is stopped and the sample is cooled down; at the D-point the sample reached a temperature of 400 °C (cooling rate: blue curve, 1 °C/s; green curve, 2 °C/s; black curve, 2.5 °C/s; red curve, 3 °C/s). The 300 μm × 300 μm optical microscopy images showing that the lower the contribution of the out-diffusion of carbon (segment CD), the lower the density of the multilayer-graphene domains.

coverage, which is however the average of the FLG graphene for a large area, is established.

Therefore, controlling the carbon coverage in relation to the graphene formation mechanism is the key issue to improve homogeneity of FLG.

We took advantage of the real-time dynamic monitoring to infer information on the graphene deposition mechanism and kinetics. Although many papers report a mechanism based on carbon segregation from the Ni bulk to the metal surface followed by precipitation growth<sup>27</sup> during the cooling stage, other papers sustain the necessity of further experimental studies to verify this mechanism, hypothesizing that direct deposition may occur simultaneously<sup>28</sup> to precipitation/segregation, as in the case of copper. Figure 5 compares the real-time kinetic data acquired during graphene deposition on Ni and Cu substrates under the same experimental conditions, showing also the possibility to monitor the process whatever the metal support. The time when CH<sub>4</sub> flows into the reactor and is stopped is also indicated. As soon as the CH<sub>4</sub> flow is turned off, heating is also stopped and the sample is cooled down at a rate of 2 °C/s. Different phenomena can be read in Figure 5. Specifically, as soon as the CH<sub>4</sub> flows into the reactor a transient region is observed for Ni, and after a critical time the observed increase of  $\langle \epsilon_1 \rangle$  is consistent with carbon in-diffusion-controlled kinetics. Interestingly, even when CH<sub>4</sub> is turned off and the Ni sample cooled down, the same trend is still observed although with a different slope, until a temperature of approximately 400 °C is reached. Below 400 °C, the  $\langle \epsilon_1 \rangle$  trend reverses and a decrease of  $\langle \epsilon_1 \rangle$  is observed. Four hundred degrees Celsius is the critical temperature above which carbon diffusion in/out of Ni bulk occurs and below which carbon diffusion is kinetically inhibited.<sup>29</sup>

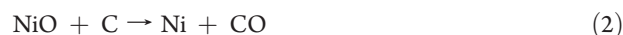
Conversely, in the case of copper, as soon as CH<sub>4</sub> is flowing a slight linear variation is seen with time until saturation is reached, and when the CH<sub>4</sub> is stopped and the sample cooled down, no further variation is observed. (Full range optical spectra for graphene on copper are shown in the Supporting Information, Figure S6). This different observed profiles can be rationalized in light of the different mechanisms for graphene growth on Ni and

Cu. Specifically, the slight variation observed for Cu is consistent with surface carbon adsorption and nucleation forming graphene at the surface which inhibits further CH<sub>4</sub>-catalyzed decomposition, yielding self-saturation of the kinetics. The flat profile recorded when CH<sub>4</sub> is off rules out any contribution of in–out diffusion and precipitation/segregation. This growth mechanism is opposite to the observed in-diffusion (line B–C in Figure 5), out-diffusion, and precipitation (line C–D in Figure 5) mechanism occurring on Ni. Therefore, the further increase of  $\langle \epsilon_1 \rangle$  when the CH<sub>4</sub> is turned off is representative of graphene formation by carbon segregation/precipitation, occurring until a temperature of 400 °C is reached cooling down.

The interesting finding in Figure 5 for Ni is the capability of discerning and controlling the contribution of both the in-diffusion (B–C in Figure 5) and out-diffusion (C–D in Figure 5) of carbon depending on the experimental parameters.

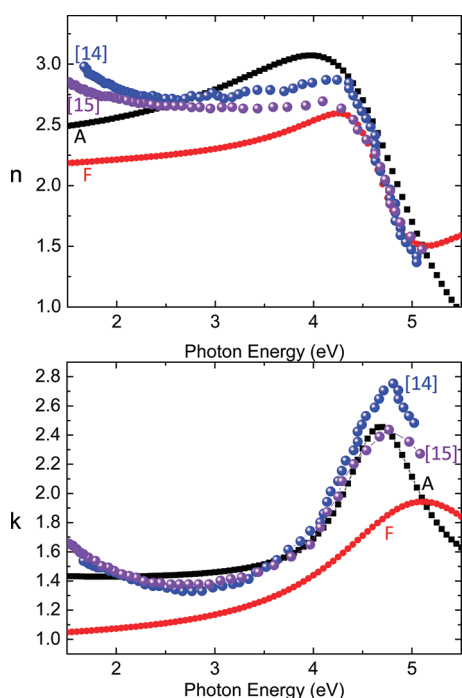
In order to have a deeper insight into the graphene formation mechanism on Ni, Figure 6 compares the real-time data acquired during graphene deposition on Ni substrates preannealed at 400 °C for different periods in the range 5–20 min, resulting in a different quality of the crystallized nickel. The time when CH<sub>4</sub> flows into the reactor and is stopped is also indicated. As soon as the CH<sub>4</sub> is off, the heating is also stopped and the sample is cooled down at a rate in the range 1–3 °C/s. In order to better understand the kinetic profiles, a simulation of the formation of a deposit of 20 Å on a Ni surface has been run and indicates that  $\langle \epsilon_1 \rangle$  should increase with increasing uptake of carbon. Furthermore, the thermal behavior during cooling of the Ni substrate and of the Ni+FLG have been preliminarily investigated to establish that a simple temperature variation from 900 °C to room temperature should be seen as a negligible decrease of  $\langle \epsilon_1 \rangle$  (see Supporting Information, Figures S4–S5).

Figure 6 shows that as soon as the CH<sub>4</sub> is turned ON a transient region exists, which depends on the status of the surface of the Ni catalyst, where chemisorption of CH<sub>4</sub> and catalytic dissociation to carbon on the surface occur. It is noteworthy that the initial point is representative of the Ni surface quality, i.e., the lower it is, the better the Ni surface (meaning better cleaning and large-grain crystallization), and independently of the initial point, the transient regime attains the same B-point, where  $\langle \epsilon_1 \rangle$  at 4.2 eV assumes the value –1 that is the value characteristic of the reference clean crystalline Ni.<sup>16</sup> Therefore, we can infer that in this transient regime, CH<sub>4</sub> is chemisorbed and dehydrogenated and both the carbon and hydrogen can contribute to the removal of residual NiO not only according to processes in eq 1 but also by



i.e., part of the carbon chemisorbed and in-diffusing through the Ni is taken in the chemical reduction of the residual NiO.<sup>30</sup> Reaction 2 competes with graphene formation, and this contributes to an uncontrolled amount of carbon in-diffusing and available for graphene formation. In fact, soon after this transient, a continuous  $\langle \epsilon_1 \rangle$  increase is observed with flowing CH<sub>4</sub>, which follows a typical diffusion profile (line B–C). Interestingly, different slopes of the  $\langle \epsilon_1 \rangle$  variation are observed depending on the initial Ni surface, the slope, i.e.,  $\Delta \langle \epsilon_1 \rangle / \Delta t$ , being a measure of the process rate. The carbon in-diffusion into Ni is governed by Fick's law

$$J_C = -D_C \frac{\partial C}{\partial x}$$



**Figure 7.** Spectra of the refractive index,  $n$ , and extinction coefficient,  $k$ , of graphene layers corresponding to samples A and F of Figure 4 of the present study (the corresponding Raman spectra are in Figure 4) compared to those of monolayer exfoliated graphene on  $\text{SiO}_2$  from ref 14 (blue dots) and of monolayer graphene from CVD after transferring to  $\text{SiO}_2$  from ref 15 (purple dots).

where  $J_C$  is the flux density of carbon,  $C$ , diffusing into Ni bulk with a diffusion coefficient  $D_C$  (which depends on temperature and is a constant in this case) and the term  $\partial c_C/\partial x$  represents the concentration gradient of carbon and is the driving force for the in-diffusion. Therefore, the observed different slope can be explained only by a different driving force  $\partial c_C/\partial x$ . From this it can be inferred that it is not the  $\text{CH}_4$  partial pressure in the gas phase governing the graphene formation rate, but rather the carbon chemisorbed on the Ni surface, which in turn depends on the Ni surface status. Specifically, the cleaner the Ni surface, the higher the reaction rate (see green curve in Figure 6, corresponding to the optimal cleaning/crystallization of Ni as discussed in Figure 2), indicating that carbon decomposition and graphene deposition rate for the first layers depend on the number of Ni sites available for the  $\text{CH}_4$  catalytic dehydrogenation and carbon chemisorptions, determining the gradient concentration and, therefore, the in-diffusion of carbon.

Interestingly, Figure 6 also shows that even when  $\text{CH}_4$  is turned off and the sample cooled down, a further  $\langle \epsilon_1 \rangle$  increase is still observed, although with a different rate, until a temperature of approximately  $400\text{ }^\circ\text{C}$  is reached (D-point in Figure 6). Below  $400\text{ }^\circ\text{C}$ , the  $\langle \epsilon_1 \rangle$  trend reverses and a slight  $\langle \epsilon_1 \rangle$  decrease is observed. The  $400\text{ }^\circ\text{C}$  is the critical temperature above which carbon diffusion in/out Ni bulk occurs and below which carbon diffusion is kinetically inhibited.<sup>29</sup> Therefore, the further increase of  $\langle \epsilon_1 \rangle$  (C–D in Figure 6) is representative of graphene formation by carbon segregation/precipitation occurring when the  $\text{CH}_4$  is turned off, until a temperature of  $400\text{ }^\circ\text{C}$  is reached cooling down. For all the kinetics in Figure 6, during the C–D segment the temperature goes from  $900$  to  $400\text{ }^\circ\text{C}$ ; i.e., a different

hydrogen pressure is experimentally used to vary the cooling rate. Interestingly, the  $\Delta\langle \epsilon_1 \rangle$  in B–C, which is indicative of the carbon out-diffusion and graphene formation, correlates with the cooling rate; i.e., the faster the cooling, the lower the  $\Delta\langle \epsilon_1 \rangle$ , providing the evidence that the cooling rate is the main parameter contributing to the graphene multilayer formation by out-diffusion and grain boundaries precipitation. In our experimental conditions, the out-diffusion is minimized for the cooling rate of  $3\text{ }^\circ\text{C/s}$  (red curve in Figure 6), which correspond to the sample that showed by Raman the largest surface fraction of monolayer regions.

Therefore, the observed kinetic profiles can be rationalized considering that (i) XRD of our crystallized Ni shows the (111) and (100) orientations; (ii) at the transient regime, the Ni(111) and Ni(100) surfaces provide sites for  $\text{CH}_4$  dehydrogenation and start to be covered with chemisorbed carbon atoms or with graphene sheets more easily than the Ni(110) surface, where the adsorbed carbon atoms are easy to diffuse away because of the lower activation energy for carbon diffusion along this direction.<sup>31</sup> The Ni (110) orientation will be kept open during carbon adsorption and diffusion, leading to the concomitant in-diffusion–precipitation–segregation.

Thus, the present approach has shown the possibility to monitor all steps involved in the graphene growth, from the metal catalyst support preparation to the carbon diffusion–segregation leading to graphene formation, and to this aim some parameters like the Ni substrate preparation have been mainly discussed. However, there are many other critical variables that can affect the graphene formation and its quality, e.g. the ratio between  $\text{CH}_4$  and  $\text{H}_2$ . Recently, Vlasiouk et al.,<sup>32</sup> analyzing by ex situ microscopy and Raman the deposition of graphene on copper by  $\text{CH}_4\text{--H}_2$ , have reported that hydrogen appears to serve a dual role, i.e., an activator of the surface bound carbon that is necessary for monolayer growth and an etching reagent that controls the size, morphology, and thickness of the graphene. Therefore, we are taking advantage of our real-time capability to explore in situ the impact of the  $\text{CH}_4\text{--H}_2$  ratio on the growth kinetics and quality of resulting graphene, which is the subject of an ongoing work. The feasibility of the real-time ellipsometry approach for also inferring the quality of graphene comes from the analysis of the exciton-interband transition absorption around  $4.6\text{ eV}$  due to a van Hove singularity in graphene's density of state. This optical criterion quality is summarized in Figure 7, where the optical constant for different graphene layers from this study (the A and F samples with the Raman mapping and spectra in Figure 4) are shown and also compared to literature data. As already discussed by Nelson et al.,<sup>15</sup> slight variations of  $n$  and  $k$  values in the visible region could differentiate low quality (lower  $n$  by nonhomogeneous and noncontinuous graphene domains) from high quality (characterized by higher  $n$ ); however, the primary criterion to assess graphene quality will be the sharpness and low broadening of the van Hove singularity absorption peak at  $4.6\text{ eV}$ . Optical data (also in the inset of Figure 4) show a sharper and narrower van Hove singularity peak for the A-spectrum, which should be closer to a monolayer, while the amplitude decreases and broadening increases with the increase of nonhomogeneity in thickness and defect.

## CONCLUSIONS

We have demonstrated a real-time monitoring method to monitor and relate all the steps involved in graphene deposition by CVD to its final thickness and quality. Specifically, we

provided a method based on spectroscopic ellipsometry, or even single-wavelength ellipsometry, to monitor (i) the cleaning and annealing of the metal catalyst, i.e., polycrystalline Ni in the present case, (ii) its impact on the carbon diffusion kinetics when CH<sub>4</sub> is injected into the CVD system, and (iii) the carbon coverage at the surface as a function of deposition parameters, which relates to graphene thickness, (iv) and to discern also the contribution of the out-diffusion/segregation during cooling down to room temperature of the graphene/Ni sample. Controlling all those steps leads ultimately to the control of graphene thickness. This technique has also been proved to be very flexible and capable of monitoring graphene formation and optical properties on a large variety of supports, including copper, opening the way for an in-line real-time graphene metrology. It has to be pointed out that although a spot size of the order 100–200 μm is available, real-time monitoring typically uses a 2 mm × 4 mm size light spot, implying that we are acquiring information on graphene quality and thickness averaged on that area. From this we can infer that accuracy on optical constants and accuracy on thickness of graphene are still an issue, also related to the nonhomogeneity of the films produced so far, which might be solved with improvements also in the CVD process on polycrystalline catalysis. Therefore, improvements in optical analysis are related to improvement in large-area graphene sample quality. Certainly, the real-time ellipsometry contributes to understanding the process and its mechanism, thereby highlighting steps to improve it in a controlled way rather than on the basis of a “trial-and-error approach”.

## ■ ASSOCIATED CONTENT

**S Supporting Information.** Picture of the experimental apparatus showing the in situ assembled ellipsometer and the ellipsometric spot on the graphene growing sample during monitoring; details and theory of the ellipsometric measurements and analysis; details of optical spectra of graphene on nickel and copper substrates and their temperature behavior. This material is available free of charge via the Internet at <http://pubs.acs.org>.

## ■ AUTHOR INFORMATION

### Corresponding Author

\*E-mail [maria.losurdo@ba.imip.cnr.it](mailto:maria.losurdo@ba.imip.cnr.it); telephone/fax +39-0805443562.

## ■ ACKNOWLEDGMENT

The authors thank Mr. Alberto Sacchetti for the technical assistance in performing growth experiments.

We also acknowledge the financial contribution of the FP7 European project NIM-NIL (GA 228637).

## ■ REFERENCES

- (1) Lin, Y. M.; Dimitrakopoulos, C.; Jenkins, K. A.; Farmer, D. B.; Chiu, H. Y.; Grill, A.; Avouris, Ph. *Science* **2010**, *327*, 662.
- (2) Berger, C.; Song, Z.; Li, X.; Wu, X.; Brown, N.; Naud, C.; Mayou, D.; Li, T.; Hass, J.; Marchenkov, A. N.; Conrad, E. H.; First, P. N.; de Heer, W. A. *Science* **2006**, *312*, 1191.
- (3) Gunlycke, D.; Areshkin, D. A.; Li, J.; Mintmire, J. W.; White, C. T. *Nano Lett.* **2007**, *7*, 3608.

- (4) Fowler, J. D.; Allen, M. J.; Tung, V. C.; Yang, Y.; Kaner, R. B.; Weiller, B. H. *ACS Nano* **2009**, *3*, 301.
- (5) Novoselov, K. S.; Geim, A. K.; Morozov, S. V.; Jiang, D.; Zhang, Y.; Dubonos, S. V.; Grigorieva, I. V.; Firsov, A. A. *Science* **2004**, *306*, 666.
- (6) Berger, C.; Song, Z.; Li, T.; Li, X.; Ogbazghi, A. Y.; Feng, R.; Dai, Z.; Marchenkov, A. N.; Conrad, E. H.; First, P. N.; de Heer, W. A. *J. Phys. Chem. B* **2004**, *108*, 19912.
- (7) Liao, K.-H.; Mittal, A.; Bose, S.; Leighton, C.; Andre Mkhoyan, K.; Macosko, C. W. *ACS Nano* **2011**, *5*, 1253.
- (8) Lee, S.; Lee, K.; Zhong, Z. *Nano Lett.* **2010**, *10*, 4702.
- (9) Li, X.; Cai, W.; An, J.; Kim, S.; Nah, J.; Yang, D.; Piner, R.; Valemakanni, A.; Jung, I.; Tutuc, E.; Banerjee, S. K.; Colombo, L.; Ruoff, R. S. *Science* **2009**, *324*, 1312.
- (10) Kim, K. S.; Houk Jang, Y. Z.; Lee, S. Y.; Kim, J. M.; Kim, K. S.; Ahn, J. H.; Kim, P.; Choi, J. Y.; Hong, B. H. *Nature* **2009**, *457*, 706.
- (11) Liu, N.; Fu, L.; Dai, B.; Yan, K.; Liu, X.; Zhao, R.; Zhang, Y.; Liu, Z. *Nano Lett.* **2011**, *11*, 297.
- (12) Lee, Y.; Bae, S.; Jang, H.; Jang, S.; Zhu, S. E.; Sim, S. H.; Il Song, Y.; Hong, B. H.; Ahn, J. H. *Nano Lett.* **2010**, *10*, 490.
- (13) Losurdo, M.; Bergmair, M.; Bruno, G.; Cattelan, D.; Cobet, C.; de Martino, A.; Fleischer, K.; Dohcevic-Mitrovic, Z.; Esser, N.; Galliet, M.; Gajic, R.; Hemzal, D.; Hingerl, K.; Humlicek, J.; Ossikovski, R.; Popovic, Z. V.; Saxl, O. *J. Nanopart. Res.* **2009**, *11*, 1521.
- (14) Kravets, V. G.; Grigorenko, A. N.; Nair, P. R.; Blake, P.; Anissimova, S.; Novoselov, K. S.; Geim, A. K. *Phys. Rev. B* **2010**, *81*, 155413.
- (15) Nelson, F. J.; Kamineni, V. K.; Zhang, T.; Comfort, E. S.; Lee, J. U.; Diebold, A. C. *Appl. Phys. Lett.* **2010**, *97*, 253110.
- (16) Palik, E. D. *Handbook of Optical Constants of Solids II*; Academic Press, Inc.: San Diego, CA, 1997.
- (17) Johnson, P. B.; Christy, R. W. *Phys. Rev. B* **1974**, *9*, 5056.
- (18) Kamineni, V. K.; Raymond, M.; Bersch, E. J.; Doris, B. B.; Diebold, A. C. *J. Appl. Phys.* **2010**, *107*, 093525.
- (19) Ostyn, K. M.; Carter, C. B. *Surf. Sci.* **1982**, *121*, 360.
- (20) Rodriguez, J. A.; Hanson, J. C.; Frenkel, A. I.; Kim, J. Y.; Perez, M. *J. Am. Chem. Soc.* **2002**, *124*, 346.
- (21) Little, J. A.; Evans, J. W.; Westmacott, K. H. *Met. Trans. B* **1980**, *11*, 519.
- (22) Yamashina, T.; Nagamatsuya, T. *J. Phys. Chem.* **1966**, *70*, 3572.
- (23) Koga, Y.; Harrison, L. G. In *Comprehensive Chemical Kinetics*; Bamford, C. H., Tipper, C. F. H., Compton, R. G., Eds.; Elsevier: Amsterdam, The Netherlands, 1984; Vol. 21, p 120.
- (24) Tomov, I.; Monev, M. *J. Appl. Electrochem.* **1992**, *22*, 262.
- (25) Fqckiewicz, A.; Poleski, M.; Palczewska, W. *J. Catal.* **1975**, *40*, 184.
- (26) Chae, S. J.; Gunes, F.; Kim, K. K.; Kim, E. S.; Han, G. H.; Kim, S. M.; Shin, H. J.; Yoon, S. M.; Choi, J. Y.; Park, M. H.; Yang, C. W.; Pribat, D.; Lee, Y. H. *Adv. Mater.* **2009**, *21*, 2328.
- (27) Li, X.; Cai, W.; Colombo, L.; Ruoff, R. S. *Nano Lett.* **2009**, *9*, 4268.
- (28) Juang, Z. Y.; Wu, C. Y.; Lu, A. Y.; Su, C. Y.; Leou, K. C.; Chen, F. R.; Tsai, C. H. *Carbon* **2010**, *48*, 3169.
- (29) Schouten, F. C.; Te Brake, E.; Gijzeman, O. L. J.; Bootsma, G. A. *Surf. Sci.* **1978**, *74*, 1.
- (30) Sharma, S. K.; Vastola, F. J.; Walker, J. R.; P., L. *Carbon* **1997**, *35*, 529–533.
- (31) Shin, Y. H.; Hong, S. *Appl. Phys. Lett.* **2008**, *92*, 043103.
- (32) Vlasiouk, I.; Regmi, M.; Fulvio, P.; Dai, S.; Datskos, P.; Eres, G.; Smirnov, S. *ACS Nano* **2011**, *5*, 6069.